CONSTRAINTS ON COMPACT STAR PARAMETERS FROM BURST OSCILLATION LIGHT CURVES OF THE ACCRETING MILLISECOND PULSAR XTE J1814-338

Sudip Bhattacharyya¹, Tod E. Strohmayer², M. Coleman Miller¹, and Craig B. Markwardt^{1,2}

ABSTRACT

Detailed modeling of the millisecond brightness oscillations from low mass X-ray binaries during thermonuclear bursts can provide us with important information about compact star parameters. Until now the implementation of this idea has not been entirely successful, largely because of the negligible amount of harmonic content in burst oscillation lightcurves. However, the recent discovery of unique, non-sinusoidal burst oscillation lightcurves from the accreting millisecond pulsar XTE J1814-338 has changed this situation. We, therefore, for the first time, make use of this opportunity to constrain compact star structure parameters effectively. In our detailed study of the lightcurves of 22 bursts we fit the burst oscillation lightcurves with fully general relativistic models that include light-bending and frame-dragging for lightcurve calculation, and compute numerically the structure of compact stars using realistic equations of state. We find that the 90% confidence interval of the dimensionless radius to mass ratio of the compact star in XTE J1814-338 is $Rc^2/GM = 3.9 - 4.9$. Our study also suggests that the observer inclination angle (measured from the upper rotational pole of the compact star) of the source is greater than 50° with very high probability. This, combined with some other known binary parameters, leads us to conclude that the secondary companion is a significantly bloated (probably due to X-ray heating) hydrogen main sequence star. We also find that the bursting hot spot on the surface of the compact star always remains large (angular radius greater than $\sim 25^{\circ}$ with 90% confidence level). Our study, for the first time, also supports the natural expectation that the photons from the thermonuclear flash come out through the layers of accreted matter under conditions of Thomson scattering.

¹Department of Astronomy, University of Maryland at College Park, College Park, MD 20742-2421; sudip@astro.umd.edu, miller@astro.umd.edu

²Laboratory for High Energy Astrophysics, Goddard Space Flight Center, NASA, Greenbelt, MD 20771; stroh@clarence.gsfc.nasa.gov, craigm@milkyway.gsfc.nasa.gov

Subject headings: equation of state — radiative transfer — relativity — stars: neutron — X-rays: binaries — X-rays: bursts

1. Introduction

Nearly coherent brightness oscillations have been discovered with the *Rossi* X-ray Timing Explorer (*RXTE*) during thermonuclear X-ray bursts from more than a dozen compact stars in low-mass X-ray binaries (Strohmayer & Bildsten 2003). The large modulation amplitudes at the onset of bursts, the time evolution of the pulsed amplitude during the rise of bursts (Strohmayer et al. 1997), the coherence of the oscillations (Smith et al. 1997; Strohmayer & Markwardt 1999; Muno et al. 2000), and the long term stability of the oscillation frequencies (Strohmayer et al. 1998) led quickly to an interpretation in terms of a "hot spot" on the surface of the star, so that the observed flux is modulated by rotation (Strohmayer et al. 1996). This interpretation has been strongly supported by observations of the transient accretion-powered pulsars SAX J1808–3658 (Chakrabarty et al. 2003) and XTE J1814–338 (Markwardt et al. 2003), in which the frequency of burst oscillations is indeed extremely close to the spin frequency as inferred from persistent oscillations.

Early on it was suggested that the intensity profiles of the pulse lightcurves contain valuable information about the stellar mass and radius (and hence about the equation of state of the dense matter in the stellar core), as well as the surface emission properties and system geometry (Strohmayer et al. 1997; Miller & Lamb 1998; Weinberg, Miller & Lamb 2001). The reason is that the lightcurves are affected by general relativistic light deflection as well as special relativistic beaming and aberration, which can be significant at the $\sim 0.1-0.2c$ linear rotational speeds implied for spin frequencies of a few hundred Hertz. However, much of the required information is encoded in the ratios of pulse amplitudes at different harmonics of the spin frequency (although some constraints can be obtained if the amplitude at the fundamental is particularly high; see Nath, Strohmayer & Swank 2002). Until recently, no source had harmonics detected definitively (for upper limits see Muno et al. 2002).

This situation has now changed. Analysis of XTE J1814–338, the fifth known accreting millisecond pulsar, shows a clear overtone in the pulse profiles of many individual bursts, with an amplitude that can be more than 0.25 times that of the fundamental (Strohmayer et al. 2003). In addition, the 314 Hz frequency of the fundamental oscillation is consistent with the spin frequency seen from the persistent pulsations. The existence of harmonics and the confirmation of the basic hot spot picture make this source very promising for detailed analysis and constraints on stellar, geometrical, and emission properties. We note that even

more precise information is in principle available from the extremely accurately characterized lightcurves of the persistent pulsations, which have several harmonics (e.g., see Cui, Morgan, & Titarchuk 1998; Poutanen & Gierliński 2003). However, the spectrum and profiles of pulses during accretion are affected by complicated details of shock physics and Comptonization. In contrast, thermonuclear burst spectra are well fit by blackbodies, without any trace of a high-energy tail related to Comptonization. They are also consistent with coming from very near the stellar surface. For these reasons, the pulses of XTE J1814–338 are most promising for an initial investigation. Combined with analyses of surface spectral line profiles (e.g., from EXO 0748-676; Cottam et al. 2002), thermonuclear X-ray bursts are key sources for constraining the state of matter inside compact stars.

Here we report our analysis of the RXTE PCA data on 22 thermonuclear bursts from XTE J1814–338. In § 2 we describe our data extraction techniques. In § 3, we discuss our theoretical models, the fitting procedure and the method of calculation of confidence intervals. We discuss our results in § 4. In particular, we show that for the three high-density equations of state (EOS) that we analyze (two nucleonic and one strange EOS), there is a preference for intermediately compact stars. We also show that the emission pattern from points on the surface is constrained strongly and is close to that expected from the law of darkening for passive radiative transport in an Thomson scattering atmosphere (Chandrasekhar 1960). In this paper we use geometric units, i.e., $G = c \equiv 1$.

2. Data Analysis

XTE J1814–338 was discovered in the Galactic bulge monitoring campaign carried out with the RXTE PCA (Markwardt & Swank 2003). The system has a binary orbital period of 4.28 hours and the compact star has a spin frequency of 314.36 Hz (Markwardt et al. 2004). This is the widest binary among the 5 known accreting millisecond pulsar systems. A total of 27 X-ray bursts were observed during the extensive RXTE follow-up of the outburst. A summary of basic burst properties can be found in Strohmayer et al. (2003). For the purposes of our modeling here we wished to produce lightcurves with as high a statistical precision as possible, while still maintaining energy resolved profiles. To do this we elected to phase-align different bursts (while preserving any misalignments among the energy bands). The energy channel boundaries were chosen so that the lightcurves in each band would have roughly similar statistical qualities (ie. similar numbers of total counts). We used the channel boundaries; 0-3, 4-6, 7-10, 11-13 and 14-28 of the "E_125us_64M_0_1s" PCA event mode. This corresponds to energy boundaries of ≈ 2 - 3.7 keV, 3.8 - 5.0 keV, 5.2 - 6.6 keV, 6.8 - 9.2 keV, and 9.4 - 23 keV. To co-add the bursts we found an offset phase for each burst

which maximized the Z_2^2 signal when adding the burst in question to the initial, reference burst. This is basically the same procedure described by Strohmayer & Markwardt (1999).

Although the different burst profiles are qualitatively similar, and hence adding them together is reasonable (see Figure 1 for added burst profile), we found that there is a general trend for the harmonic strength to decrease with time. That is, bursts occurring later in the outburst seem to have somewhat smaller ratios of the first harmonic amplitude to that at the fundamental. This suggests that some secular change associated with the accretion rate might be influencing the details of the pulse profiles. Therefore, to allow for such changes while still obtaining good statistics, we elected to add together the bursts in three groups based on their times of occurrence. Since the overall structure (ie. the mass and radius) of the compact star must remain fixed through the outburst, the secular changes in the pulse profile may reflect small changes in the spot size, location or perhaps beaming function, with time. We will say more about this shortly.

3. Physical Effects and Calculations

The basic picture we employ is one in which photons from the surface of the star propagate freely in vacuum to the observer. This approach ignores any scattering during the propagation. If there were scattering by a hot plasma near the star, we would expect this to leave its Comptonization imprint on the spectrum as an extended power-law tail. The lack of such a signature (Strohmayer et al. 2003) supports the assumption of free propagation.

Even with this simplification, if the emission pattern on the surface and the angledependence of specific intensity from a given point on the surface are arbitrary, then there are too many free parameters and no meaningful constraints are possible. Therefore, to make progress in modeling, we adopt the following assumptions:

- The surface consists of a background of uniform intensity and spectrum, plus a single hot spot that is a filled circle that emits uniformly.
- The hot spot does not overlap either rotational pole. This assumption allows simplifications in the numerical procedure.
- The minimum value of R/M is 3.6, again to simplify numerical techniques by ensuring that no emitted photon is deflected by more than 180° .

With these assumptions, we calculate lightcurves by tracing rays backwards, i.e., from the observer to the stellar surface. The paths of these rays, and their specific intensities, carry the imprint of several physical effects. In this paper, we consider: (1) Doppler boosts, (2) special relativistic beaming, (3) gravitational redshift, (4) light-bending, and (5) frame-dragging. We do not include the effects of spin-induced stellar oblateness. These effects are only second order in the stellar rotation and are thus small compared to other uncertainties. For example, for all our EOS models, the polar to equatorial radii ratio of the star is greater than 0.98 (for stellar mass $M \geq 1.4 M_{\odot}$ and observed stellar spin frequency $\nu_* \sim 314 \text{ Hz}$).

To make our model lightcurves realistic, we calculate the relation between M and the stellar radius R, as well as a/M (where, a is the stellar angular momentum per unit mass) for a given M and ν_* (~ 314 Hz for XTE J1814-338), with a specified EOS model. We do this by computing numerically the stable structure of a rapidly spinning compact star, using the formalism given by Cook, Shapiro & Teukolsky (1994) (see also Bhattacharyya et al. 2000 for a detailed description). For a particular compact star EOS model and assumed values for the stellar mass and spin rate, we solve Einstein's field equations and the equation of hydrostatic equilibrium self-consistently to obtain other stellar structure parameters (radius, angular momentum, etc.). We use these output parameters in our timing calculations.

In our detailed lightcurve calculation, we have five input parameters, for a given EOS model and the known value of ν_* . In our study, the structure of the star is fixed by one unknown parameter, which we choose to be (1) the dimensionless stellar radius to mass ratio (R/M). The hot spot is specified by two parameters: (2) the θ -position θ_c of the center of the spot, and (3) the angular radius $\Delta\theta$ of the spot. The emission from a single point on the spot, as measured in the corotating frame, is characterized by (4) a parameter n that gives a measure of the beaming in emitter's frame, where the specific intensity as a function of the angle ψ from the surface normal is $I(\psi) \propto \cos^n(\psi)$. Finally, we have (5) the inclination angle i of the observer as measured from the upper rotational pole. It is to be noted, that at the initial phase of our model calculation, we consider that the hot spot emits as a blackbody (as burst spectra can be fitted well by blackbodies) with a temperature kT = 2 keV. However, later we allow the source spectrum to deviate from a blackbody (for discussion about the spectrum and the justification of the assumed temperature, see later in this section).

In our work, we consider three representative EOS models: two for neutron stars and one for strange stars (made completely of u, d and s quarks). The neutron star EOS models are A18 and A18+ δv +UIX (Akmal et al. 1998). The first one is the Argonne v_{18} model (Wiringa, Stoks & Schiavilla 1995) of two-nucleon-interaction. This model fits the Nijmegen database (Stoks et al. 1993) with $\chi^2/N_{\rm data} \sim 1$, and hence is called "modern". The model A18+ δv +UIX considers two additional physical effects: the three-nucleon-interaction (Urbana IX (UIX) model; Pudliner et al. 1995) and the effect of relativistic boost corrections to the A18 interaction. The phenomenological strange star EOS model B90 is a MIT bag

model for massless, non-interacting quarks with the bag constant $B = 90 \text{ MeV/fm}^3$ (Farhi & Jaffe 1984). The EOS models A18 and B90 are soft, i.e., the maximum non-rotating mass they support is small ($\sim 1.6 - 1.7 M_{\odot}$). On the other hand, the EOS model A18+ δv +UIX is stiff (maximum supported non-rotating mass is $\sim 2.2 M_{\odot}$). Figure 2 shows the stable stellar mass vs. radius curves for these EOS models (for stellar spin frequency $\sim 314 \text{ Hz}$). Although, there are many EOS models available in literature, that we are not considering, the diversity of our chosen EOS models enhances the generality of our results.

In order to compute the energy dependent flux, we trace back the path of the photons from the observer to the hot spot, using the Kerr space-time. This ray-tracing enables us to get the boundary of the image of the source at the observer's sky. We then calculate the observed flux by integrating the observed energy dependent specific intensity inside the boundary of this image (for a detailed description, see Bhattacharyya, Bhattacharya & Thampan 2001). The model lightcurve is calculated by repeating the same procedure for many spots at different ϕ -positions on the surface of the star.

In this paper, we compare our models with the data of 22 bursts. Based on burst occurrence time and the harmonic strength of the lightcurves, as described above, we added all the bursts in three groups; bursts 1-8; 9-16; and 17-22. We phase-align and stack the bursts within each group, and therefore effectively analyze three characteristic sets of pulse profiles. We used five energy bands for each group. The energy ranges are given in §2 above.

We compare our models directly with the data. To do this, we compute a model lightcurve of intensity and spectrum versus pulse phase. In this initial step we consider only the lightcurve of the hot spot, not any background emission. We fold the model spectrum through the RXTE response matrix to get counts per channel as a function of rotational phase. For each channel range, we then add a phase-independent background (which is a free parameter) and normalize it so that the total number of counts in that channel range, summed over all phases, is the same as the number of counts in that channel range in the observed lightcurve. Our final step is to shift the entire lightcurve in phase (by same amount for all the channel bands) to maximize the match with the observed lightcurve, as determined by a χ^2 statistic.

The procedure of adding backgrounds and normalizing counts independently in each of the channel ranges has two implications. First, the independent backgrounds mean that we leave the unpulsed spectrum unconstrained. Second, the independent normalizations mean that although we calculate the initial spectrum and lightcurve of the hot spot assuming a kT = 2 keV blackbody, renormalization allows the effective spectrum to deviate from blackbody. Therefore, only the rms variability of a blackbody with, e.g., Doppler shifts is preserved, and not the whole spectrum. We justify this because, in reality, we do not expect

the temperature to be constant throughout a hot spot; for example, if the hot spot is related to a magnetic pole, it might be hotter in the center than at the edges. In addition, the pulse profiles extracted from the observations incorporate data over a period of several 10s of seconds, during which the hot spot is likely to cool significantly. Thus, the time-averaged spectrum will not truly be a blackbody, hence we let the spectrum be adjusted by allowing independent normalizations.

The initially chosen hot spot temperature of 2 keV is justified for the following reasons:

1. It is expected to be close to the average blackbody temperature of the hotspot for most of the bursts (see Kuulkers et al. 2003 for blackbody temperature variation during burst evolution for several sources), and 2. The likelihood distributions (see next two paragraphs for description) for the parameters are similar, even for widely different initially chosen hot spot temperatures.

Using the above procedure of adding backgrounds, normalizing, and shifting phases, we find the best χ^2 value for many different combinations of parameters. To be systematic, we consider combinations of parameters on a grid (for the values of each parameter, see Table 1). The number of counts per phase bin in each channel range is large enough that Gaussian statistics apply, hence the likelihood is proportional to $\exp[-\chi^2/2]$.

Once the likelihoods are computed for each combination of parameters, we produce likelihoods for each parameter individually via the process of marginalization. In this process, let the posterior probability density over the full set of model parameters $\theta_1 \dots \theta_n$ be $p(\theta_1 \dots \theta_n)$. If we are interested in the credible region for a single parameter θ_k , then we integrate, or marginalize, this probability distribution over the "nuisance" parameters $\theta_1 \dots \theta_{k-1}$ and $\theta_{k+1} \dots \theta_n$:

$$q(\theta_k) = \int d\theta_1 \dots d\theta_{k-1} d\theta_{k+1} \dots d\theta_n p(\theta_1 \dots \theta_n) . \tag{1}$$

For our purposes we assume that each combination of parameters has the same a priori probability, hence the posterior probability is simply proportional to the likelihood. For Gaussian distribution of likelihoods of a parameter, this method is equivalent to the standard frequentist procedure. However, for non-Gaussian distribution, our method is more general.

We find that the posterior probability distributions are not Gaussian for most of our parameters. Therefore, although there is a unique maximum likelihood value for any parameter, credible regions cannot be quoted uniquely. For example, one gets a different value if one assumes a symmetric distribution than if one looks for the smallest region containing a certain total probability. We have adopted a variant of the latter procedure. Using linear interpolations of the probability between grid points for a given parameter, we compute the smallest region that includes the maximum likelihood points and contains 90% of the total

probability. For parameters expected to remain unchanged between bursts (specifically, R/M and the observer inclination i) we combine data from all bursts. For the other parameters, we calculate likelihoods separately for each of the three burst groups.

4. Results and Conclusions

As discussed in \S 3, we perform comparisons using three EOS models. For neutron star EOS models, the minimum value of R/M we consider is 3.6, whereas for the strange star EOS model, this value is 3.7, as for a stable stellar structure, a lower value is not possible for this EOS model. Although this prevents a direct likelihood comparison of all the EOS models, it still allows a likelihood comparison of the values for a given parameter for a particular EOS model.

Figure 3 shows the goodness of fit for a certain burst group and channel range, and for a plausible combination of parameter values. The χ^2 value for this example comes out to be ~ 24.5 , for the number of degrees of freedom equal to 24. This goodness of fit suggests that the overall model framework is a reasonable representation of the data. However, for certain burst group and channel range combinations, the lowest possible χ^2 value can be greater than 30 (for 24 degrees of freedom).

In Figure 4, we plot the likelihoods with the parameter R/M, for three EOS models, using the data from all 22 bursts. For the neutron star EOS models A18+ δv +UIX and A18, the likelihood peaks at R/M=4.2, whereas for the strange star EOS model B90, the peak is at R/M=4.5. Despite the differences between the EOS models, the likelihood distributions are very similar, suggesting that the inferred results are robust. It also shows that the minimum computed value (i.e., 3.6) of R/M does not introduce any bias in our conclusions.

We plot the normalized probability distribution for the observer inclination angle i in Figure 5, using all 22 bursts. Curves for all the EOS models show that a value less than 50° is highly improbable, but higher angles (i.e., observer lines of sight closer to the rotational equator) are not easily distinguishable. Our work does suggest that the system is not close to face-on, which means that the companion mass is reasonably well constrained by the pulsar mass function.

The observed value of pulsar mass function and orbital period for this source are $0.002016\,M_{\odot}$ and 4.27 hours respectively (Markwardt, Strohmayer & Swank 2003). Hence, a reasonable range $(1.4\,M_{\odot}-2.0\,M_{\odot})$ of compact star mass M and a lower limit $50^{\rm o}$ of i imply a companion mass range $0.17\,M_{\odot}-0.29\,M_{\odot}$. Therefore, for the observed orbital period, the

companion can neither be a helium main sequence star, nor a degenerate star (Bhattacharya & van den Heuvel 1991). It is also too large to be a brown dwarf (as was predicted for another accreting millisecond pulsar system SAX J1808.4-3658; Bildsten & Chakrabarty 2001). The most probable option is that it is either a hydrogen main sequence star, or an evolved (sub-)giant star. However, the companion mass is too small for it to have evolved off the main sequence (Böhm-Vitense 1992). Therefore, the most likely option is a hydrogen main sequence star. Interestingly, the stellar radius (assuming there is Roche lobe overflow) is too big for a normal hydrogen main sequence star. For example, for the upper limit of mass and lower limit of observer's inclination angle, the companion radius is about 40% bigger than the normal radius (Bhattacharya & van den Heuvel 1991), and it is even bigger for a smaller companion mass. Therefore, we conclude that the companion is bloated, probably due to X-ray heating by the compact star. Figure 8 shows this directly in the companion radius vs. mass plane.

In Table 2, we give the range of R/M and i that includes 90% of the probability, for each of the three EOS models. We find that, the 90% confidence interval of R/M (union for all three EOS models) is 3.9 - 4.9, and with the same (i.e., 90%) confidence level, the lower limit of the inclination angle i is $\sim 70^{\circ}$ for all three EOS models. However, the upper limit of the inclination angle is not constrained.

In Table 3, we display the 90% confidence intervals for the θ -position of the center of the hot spot (θ_c) and its angular radius $(\Delta\theta)$ for all the EOS models. Here we give the results for the three burst groups separately, as the values of these two parameters may change from one group to another. The peak of the likelihood distribution for θ_c always occurs around the interval $50^{\circ} - 90^{\circ}$, and its lower limit with 90% confidence level is typically $\gtrsim 30^{\circ}$. The upper limit of $\Delta\theta$ is not constrained, as the maximum value that we consider, is 60° . However, its lower limit (with 90% confidence level) is in general $\gtrsim 25^{\circ}$. This suggests that the spot remains large for all the bursts.

The beaming parameter n (defined in § 3) peaks at n=0.6 (if we consider four values of n, mentioned in Table 4) for all the burst groups and all the EOS models. Therefore we combine the likelihoods for all three burst groups in Table 4. This table demonstrates that the likelihood distribution of n is similar for all the EOS models, and that the actual value of n is close to 0.6. We, therefore, calculate the likelihood distribution for 30 values of n for three EOS models. This is shown in Figure 6. The similarity in these distributions for all the EOS models, shows the robustness of our results. The likelihood peaks at n=0.6 for the EOS model A18+ δv +UIX and the 90% confidence interval (union for all three EOS models) is 0.45-0.81.

The physical interpretation of these values of n is the following. The thermonuclear

flash is expected to occur at the bottom of a pile of accreted matter. Therefore, although the original emission may be isotropic, what comes out through the layers of accreted matter should be beamed. The law of darkening (i.e., the angular distribution of specific intensity) for semi-infinite plane-parallel layers with a constant net flux and Thomson scattering, is given in Chandrasekhar (1960). In Figure 7, we compare this law of darkening $I(\psi)$ with our emission function $\cos^n(\psi)$. We find that, for n = 0.5 (which is within the 90% confidence interval), our emission function matches with the $I(\psi)$ quite well, except for nearly tangential emission (for which the emitted flux is small). The matching is also reasonably good for the most probable value (for the EOS model A18+ δv +UIX) n = 0.6. Therefore, it is quite possible that the actual emission is through the layers of accreted matter and under conditions of Thomson scattering (by thermal electrons). Such an interpretation explains the beaming in a natural way, without requiring a strong magnetic field.

Finally, in Table 5, we compare the likelihoods of two neutron star EOS models, by summing the likelihoods of all the parameter combinations, and using data from all 22 bursts. As the total likelihood comes out to be similar for the two EOS models, we can not distinguish the EOS models in this way.

In conclusion, the significant overtones observed in the pulse profiles of burst brightness oscillations from XTE J1814–338 open up new possibilities for constraints on compact star structure as well as on source geometry and emission properties. We find that fairly compact stars are favored by the data, and that the beaming pattern from points on the surface is quite close to that expected from radiative transport in a static, plane-parallel scattering atmosphere. It is likely that in the future, more millisecond burst oscillations with non-sinusoidal lightcurves will be observed from other X-ray sources. With future generation X-ray satellites (for example, Constellation-X, or a future large area timing mission) with higher detector area and sufficient time resolution, such lightcurves will provide tight constraints on models of stellar structure.

We thank Arun V. Thampan for providing the rapidly spinning compact star structure calculation code, and Geoff Ravenhall for supplying the nucleonic equation of state data. Many of the results in this paper were obtained using the Beowulf cluster of the department of astronomy, University of Maryland (courtesy of Derek C. Richardson). This work was supported in part by NSF grant AST 0098436.

REFERENCES

Akmal, A., Pandharipande, V.R., & Ravenhall, D.G. 1998, PRC, 58, 1804

Bhattacharya, D., & van den Heuvel, E.P.J. 1991, Physics Reports, 203, 1

Bhattacharyya, S., Bhattacharya, D., & Thampan, A.V. 2001, MNRAS, 325, 989

Bhattacharyya, S., Thampan, A.V., Misra, R., & Datta, B. 2000, ApJ, 542, 473

Bildsten, L. & Chakrabarty, D. 2001, ApJ, 557, 292

Böhm-Vitense, E. 1992, Introduction to stellar astrophysics: vol. 3, Cambridge University Press

Chakrabarty, D. et al. 2003, Nature, 424, 42

Chandrasekhar, S. 1960, Radiative Transfer, Dover Publications

Cook, G.B., Shapiro, S.L., & Teukolsky, S.A. 1994, ApJ, 424, 823

Cottam, J., Paerels, F., & Mendez, M. 2002, Nature, 420, 51

Cui, W., Morgan, E.H., & Titarchuk, L.G. 1998, ApJ, 504, L27

Farhi, E., & Jaffe, R.L. 1984, Phys. Rev. D, 30, 2379

Kuulkers, E., den Hartog, P.R., in't Zand, J.J.M., Verbunt, F.W.M., Harris, W.E., & Cocchi, M. 2003, A&A, 399, 663

Markwardt, C.B. et al. 2004, in preparation

Markwardt, C.B., Strohmayer, T.E., & Swank, J.H. 2003, ATEL, 164

Markwardt, C.B., & Swank, J.H. 2003, IAUC, 8144

Markwardt, C.B., Swank, J.H., Strohmayer, T.E., in 't Zand, J.J.M., & Marshall, F.E. 2002, ApJ, 575, L21

Miller, M.C., & Lamb, F.K. 1998, ApJ, 499, L37

Muno, M.P., Fox, D.W., Morgan, E.H. & Bildsten, L. 2000, ApJ, 542, 1016

Muno, M.P., Özel, F., & Chakrabarty, D. 2002, ApJ, 581, 550

Nath, N.R., Strohmayer, T.E., & Swank, J.H. 2002, ApJ, 564, 353

Poutanen, J., & Gierliński, M. 2003, MNRAS, 343, 1301

Pudliner, B.S., Pandharipande, V.R., Carlson, J., & Wiringa, R.B. 1995, Phys. Rev. Lett., 74, 4396

Rappaport, S., & Joss, P.C. 1984, ApJ, 283, 232

Smith, D., Morgan, E.H. & Bradt, H.V. 1997, ApJ, 479, L137

Stoks, V.G.J., Klomp, R.A.M., Rentmeester, M.C.M., & de Swart, J.J. 1993, Phys. Rev. C, 48, 792

Strohmayer, T.E. et al. 1996, ApJ, 469, L9

Strohmayer, T.E. et al. 1998, ApJ, 503, L147

Strohmayer, T.E., & Bildsten, L. 2003, in *Compact Stellar X-ray Sources*, Eds. W.H.G. Lewin and M. van der Klis, (Cambridge University Press: Cambridge), (astro-ph/0301544)

Strohmayer, T.E., & Markwardt, C.B. 1999, ApJ, 516, L81

Strohmayer, T.E., Markwardt, C.B., Swank, J.H., & in 't Zand, J. 2003, ApJ, 596, L67

Strohmayer, T.E., Zhang, W., & Swank, J.H. 1997, ApJ, 487, L77

Verbunt, F. 1990, in *Neutron Stars and Their Birth Events*, Ed. W. Kundt, (Kluwer Academic Publishers, Dordrecht)

Weinberg, N., Miller, M.C., & Lamb, D.Q. 2001, ApJ, 546, 1098

Wiringa, R.B., Stoks, V.G.J., & Schiavilla, R. 1995 Phys. Rev. C, 51, 38

This preprint was prepared with the AAS IATEX macros v5.2.

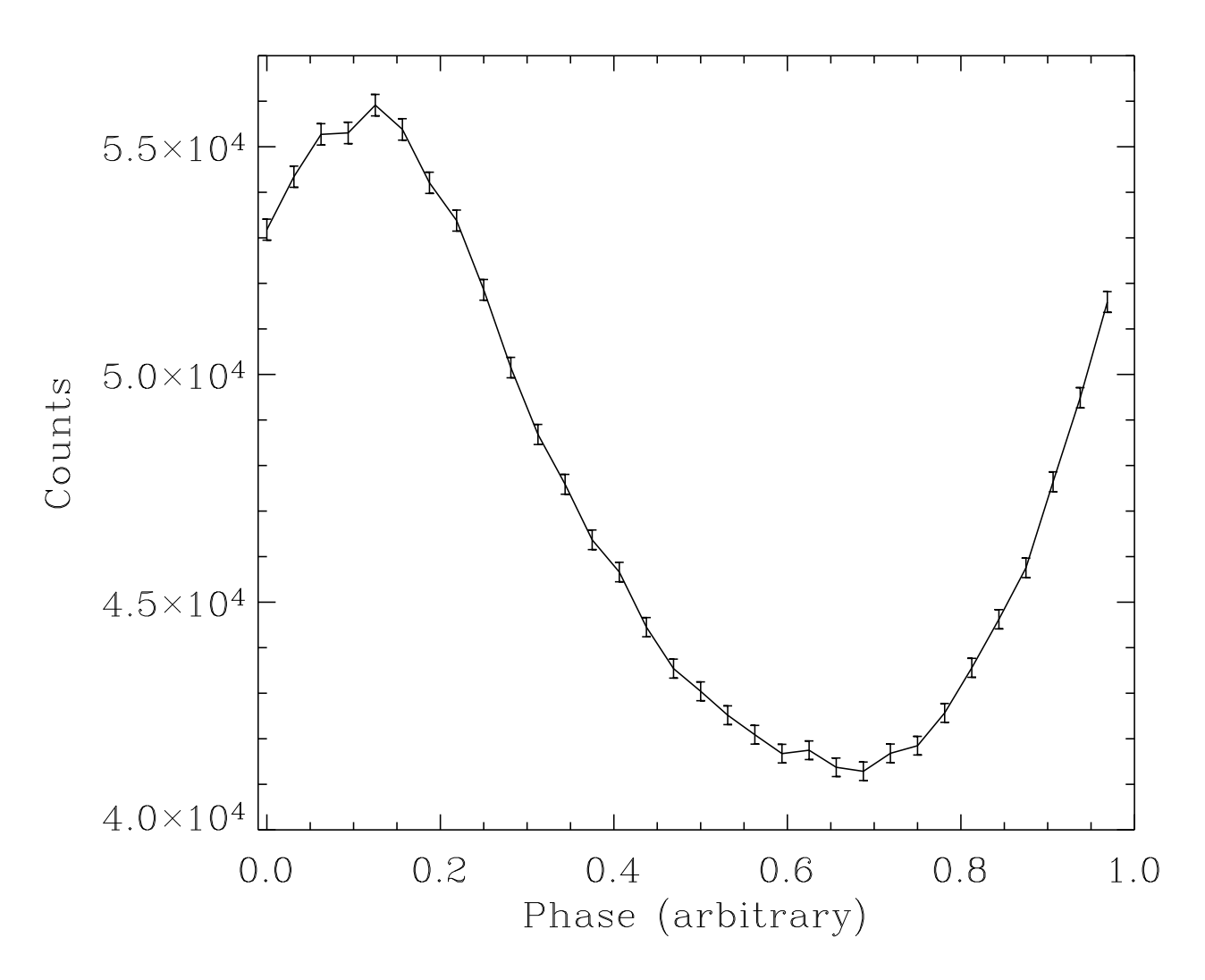


Fig. 1.— The fully added observational lightcurve (22 bursts and 0-28 channels)

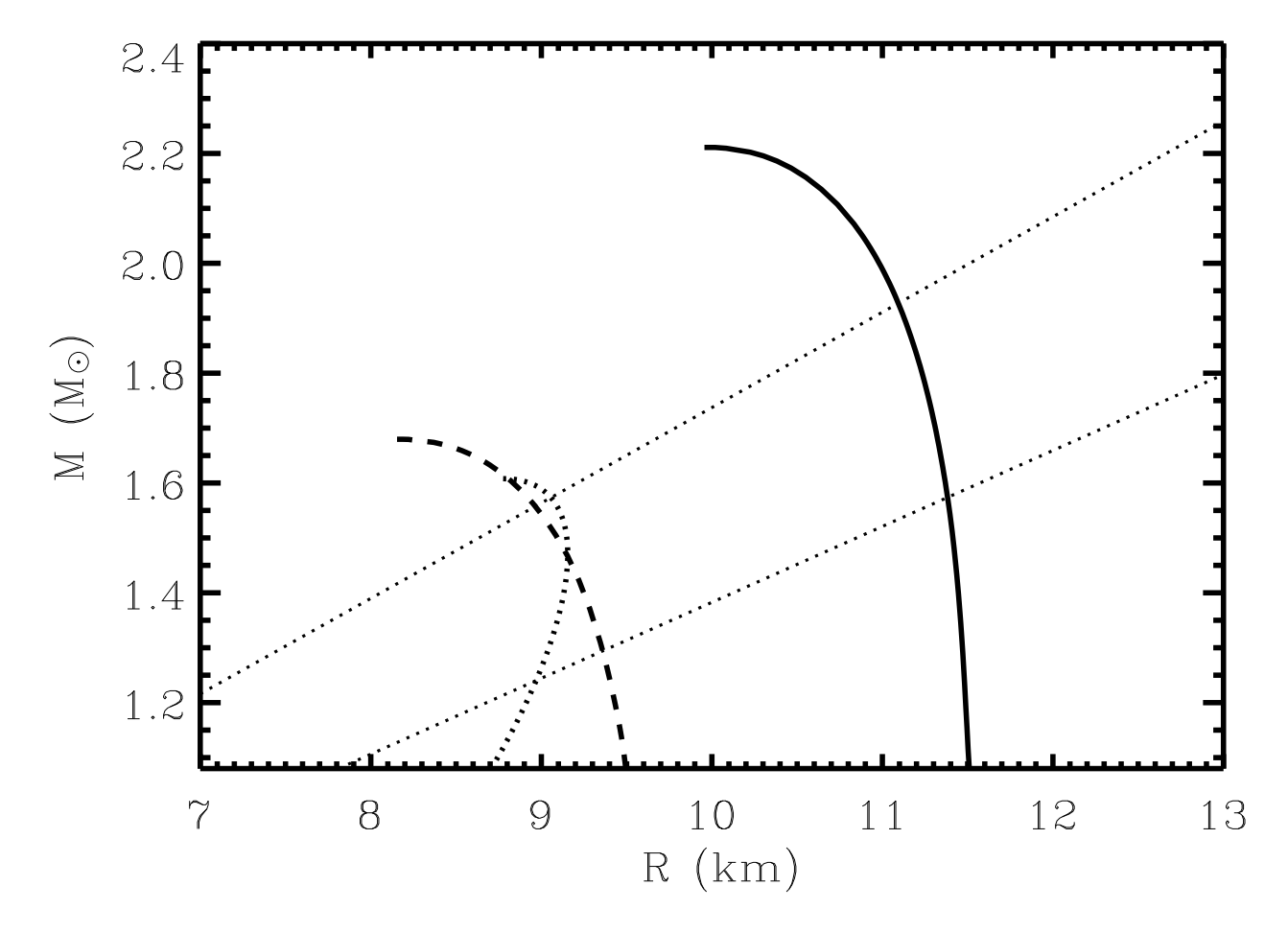


Fig. 2.— Mass vs. radius diagrams: The solid curve is for the EOS model A18+ δv +UIX (for neutron star), the dashed curve is for the EOS model A18 (for neutron star), and the thick dotted curve is for the EOS model B90 (for strange star). These diagrams are for stable stellar configurations, spinning with a frequency ~ 314 Hz. The two inclined dotted lines (corresponding to the vertical dotted lines of Figure 4) give the 90% confidence interval of R/M (union for all three EOS models). These lines constrain the mass vs. radius plane for the compact star in XTE J1814-338.

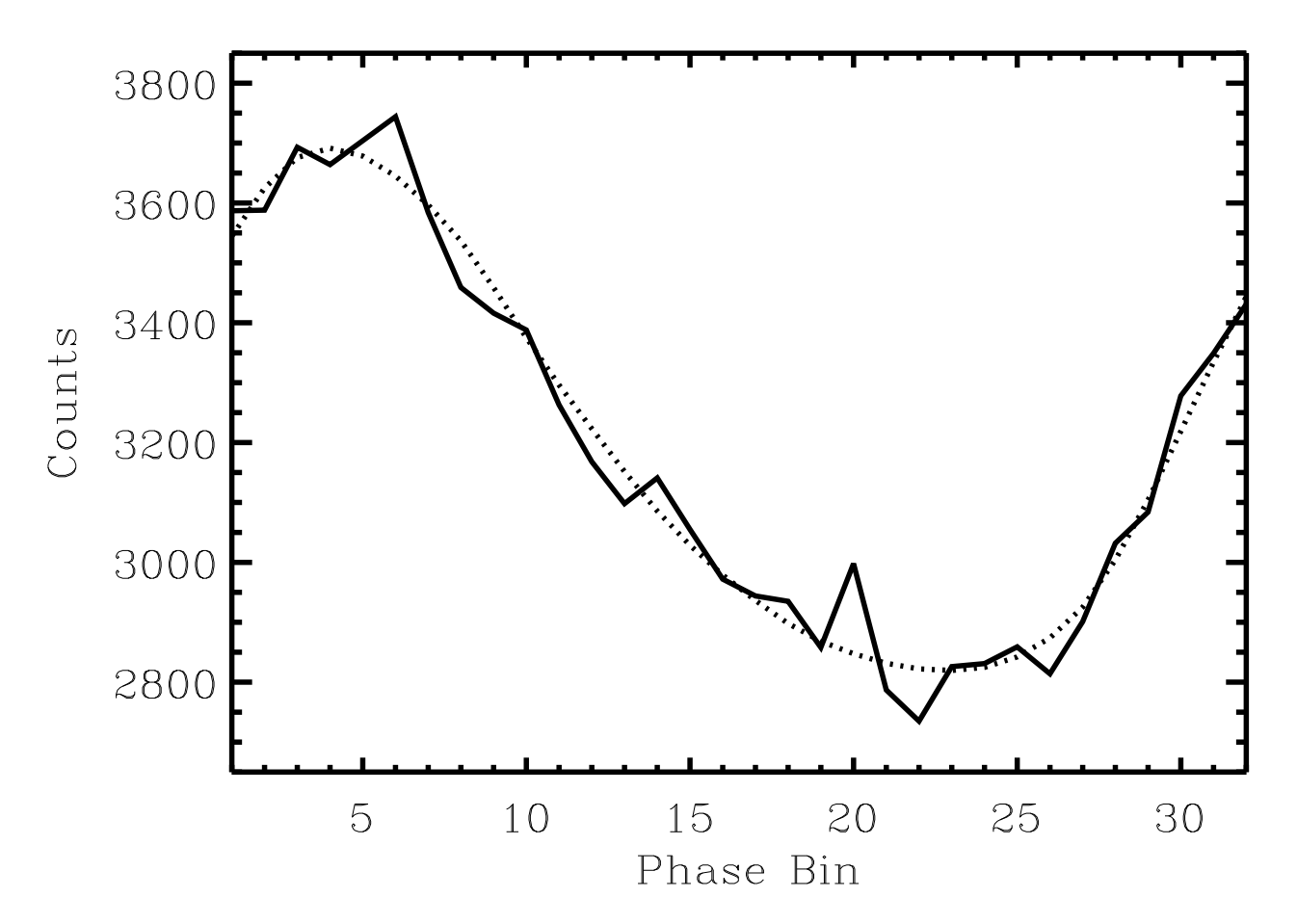


Fig. 3.— A representative good fit to the data. Stacked data (solid curve) for bursts 1-8 (channel range: 11-13) from XTE J1814-338, versus a model (dotted curve) in which $R/M=4.0,\ i=75^{\circ},\ \theta_{\rm c}=90^{\circ}$, the hot spot has an angular radius of $45^{\circ},\ n=0.5$, and $T_{\rm BB}=2.0$ keV (see text for description of parameters). Here we have used the EOS model A18+ δv +UIX. In this fitting we get a χ^2 value ~ 24.5 , for the number of degrees of freedom equal to 24.

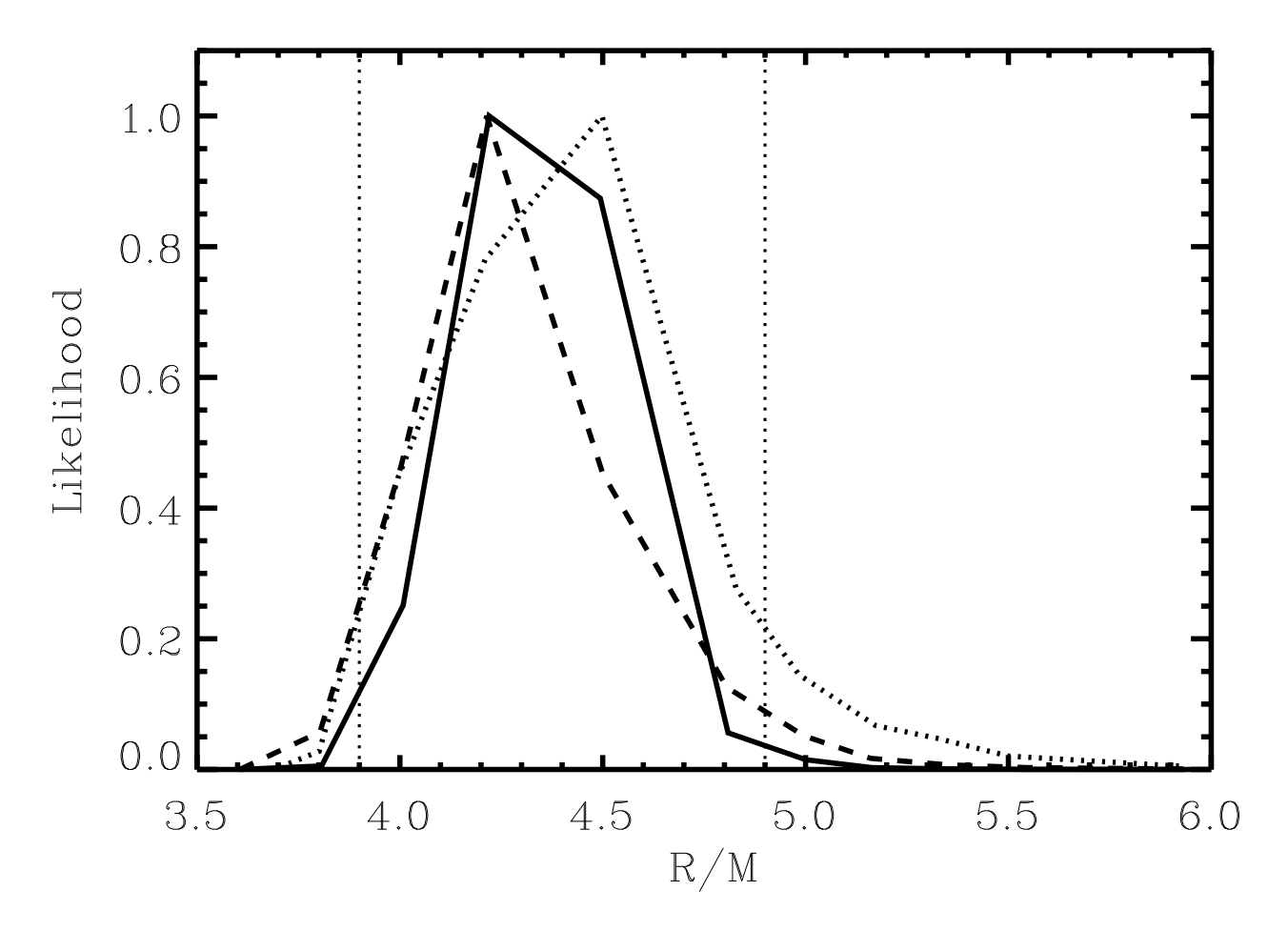


Fig. 4.— Likelihood distribution of stellar radius to mass ratio R/M, using data from all 22 bursts. The solid curve is for the EOS model A18+ δv +UIX (for neutron star), the dashed curve is for the EOS model A18 (for neutron star), and the thick dotted curve is for the EOS model B90 (for strange star). The two vertical dotted lines give the 90% confidence interval (union for all three EOS models).

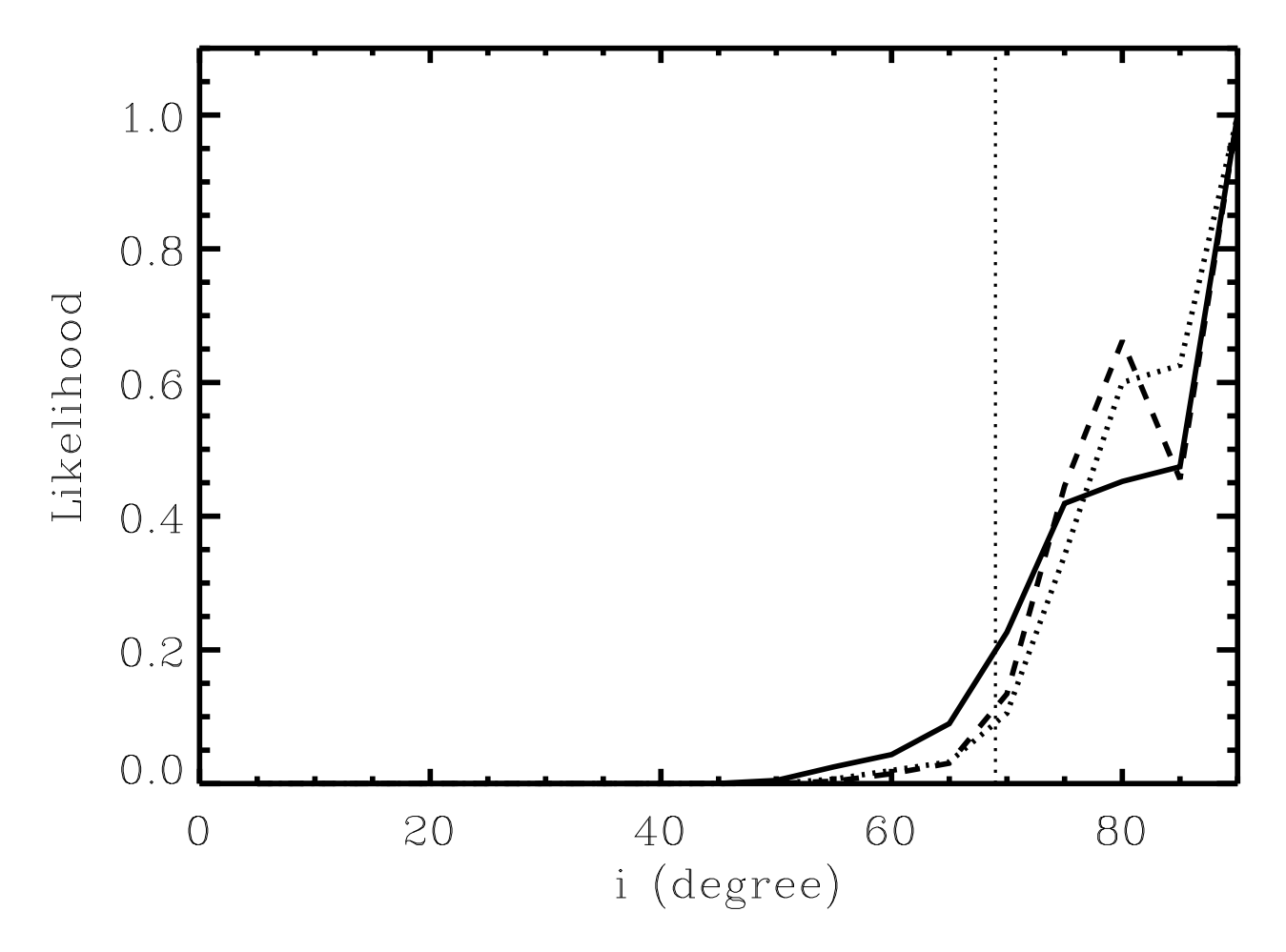


Fig. 5.— Likelihood distribution of observer's inclination angle i, using data from all 22 bursts. Solid curve is for the EOS model A18+ δv +UIX (for neutron star), the dashed curve is for the EOS model A18 (for neutron star), and the thick dotted curve is for the EOS model B90 (for strange star). The vertical dotted line gives the lower limit of 90% confidence interval (union for all three EOS models). This figure shows that a value of i less than 50° is highly improbable.

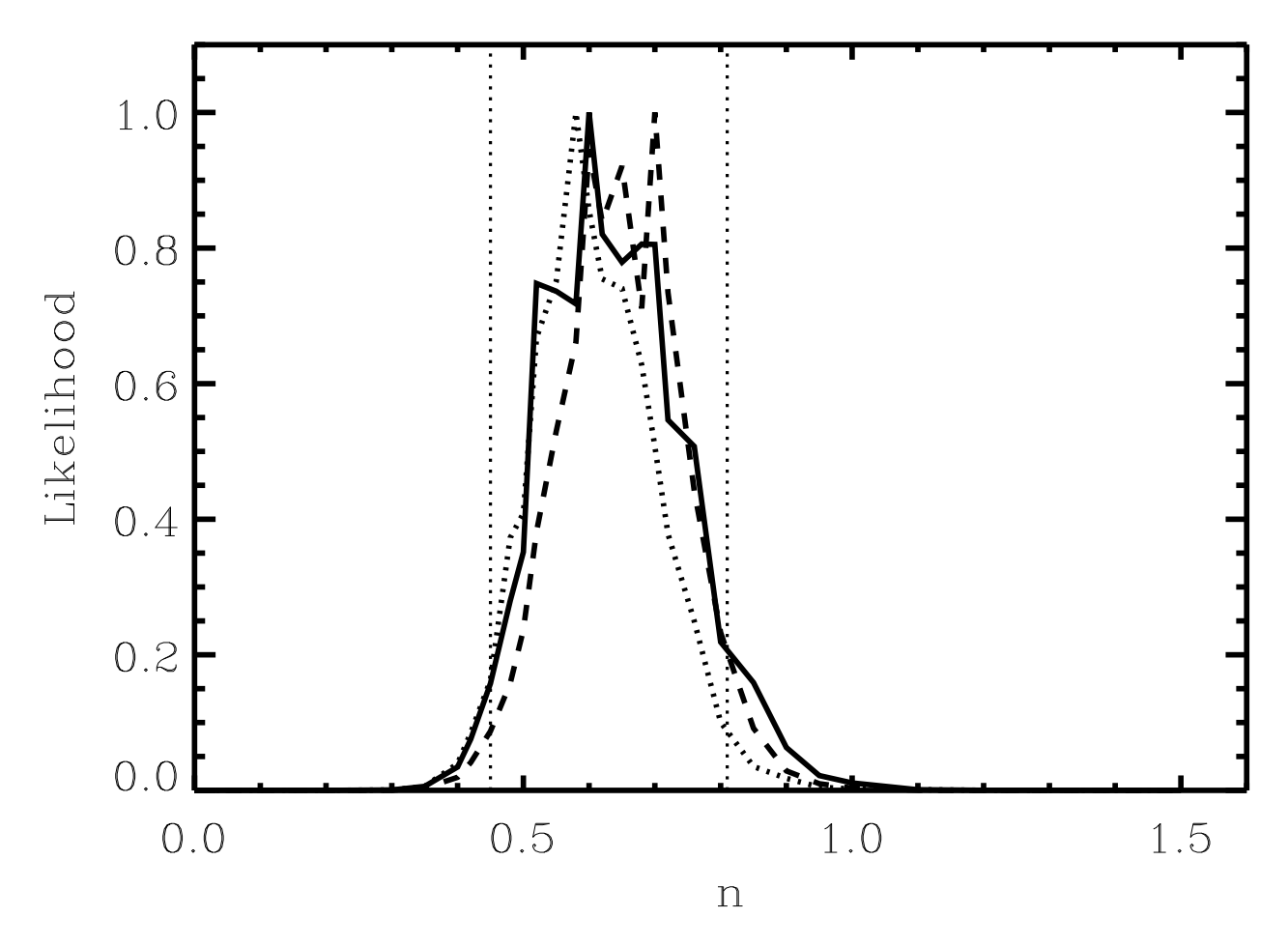


Fig. 6.— Likelihood distribution of the beaming parameter n (defined in § 3), using data from all 22 bursts. The solid curve is for the EOS model A18+ δv +UIX (for neutron star), the dashed curve is for the EOS model A18 (for neutron star), and the thick dotted curve is for the EOS model B90 (for strange star). The two vertical dotted lines give the 90% confidence interval (union for all three EOS models). This figure gives a well constrained emission pattern.

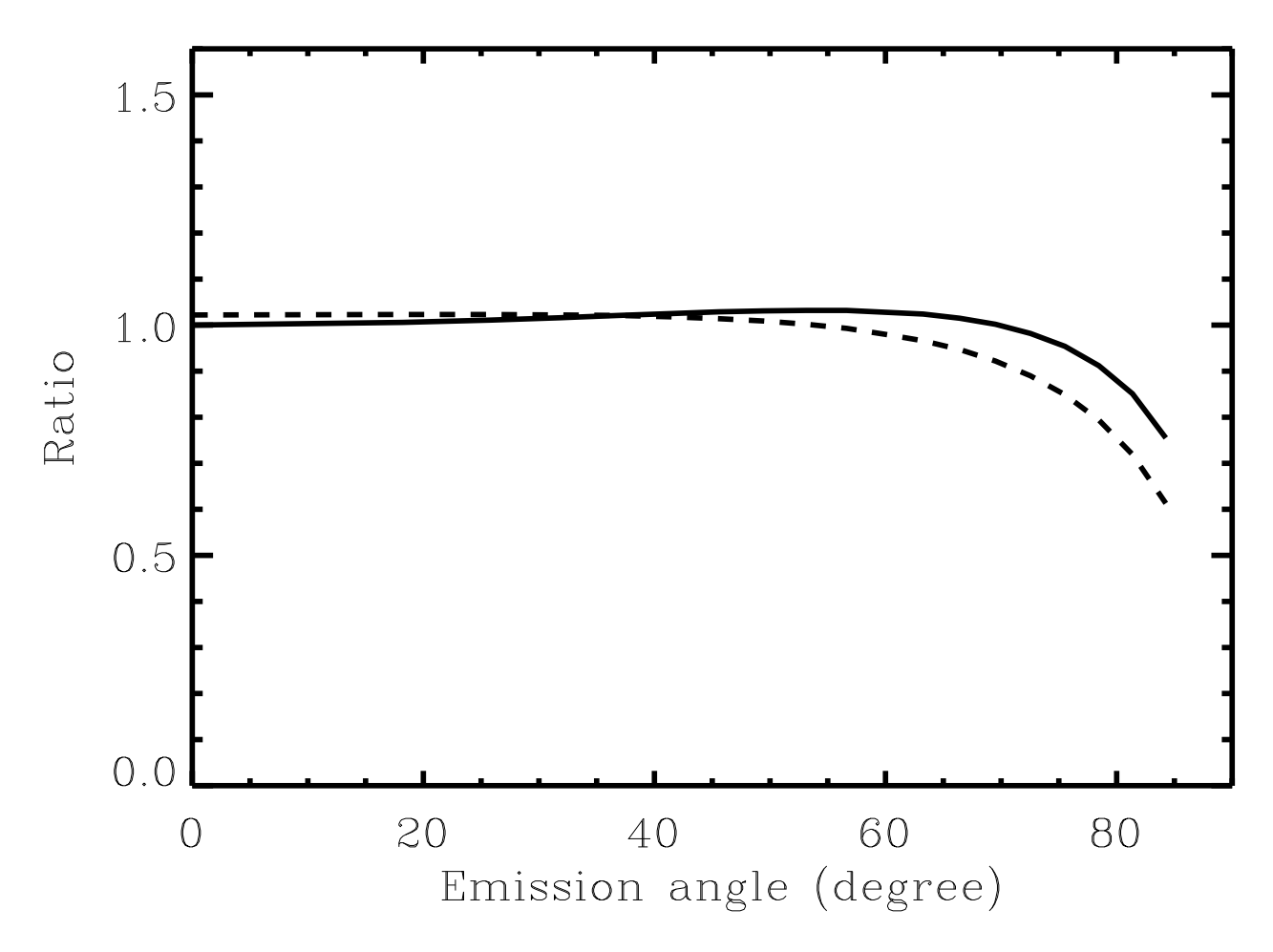


Fig. 7.— Comparison between $I(\psi)$ (Law of darkening; Chandrasekhar 1960) and our emission function $(\cos^n \psi)$: Both the functions give the angular distribution of specific intensity in emitter's frame. Here the independent parameter is the emission angle (ψ) in emitter's frame (measured from surface normal), and the dependent parameter is the ratio of $A\cos^n(\psi)$ to $I(\psi)$ (where, A is an arbitrary constant, and $I(\psi)$ is the law of darkening for the radiative transfer in a semi-infinite plane-parallel atmosphere with a constant net flux and Thomson scattering). The solid curve is for n = 0.5, and the dashed curve is for n = 0.6. For both the cases, $I(\psi)$ is well fitted by our emission function, except for very high emission angle, for which the emitted flux is small.

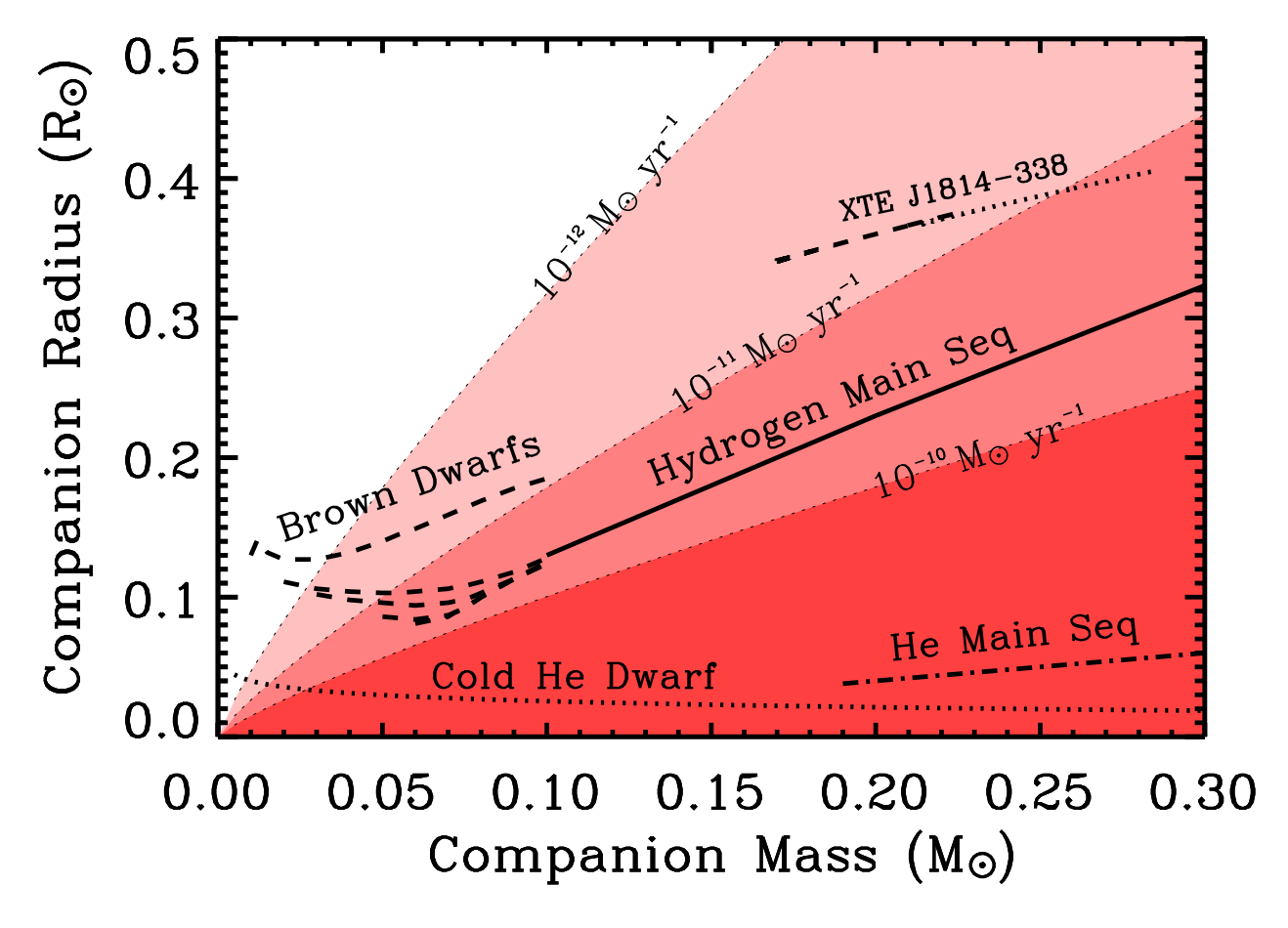


Fig. 8.— Companion mass vs. radius plane (similar to the Figure 4 of Markwardt et al. 2002): The lines under the phrase 'XTE J1814-338' are for the companion star in the source XTE J1814-338 (for an observer inclination angle in the range $50^{\circ} - 90^{\circ}$); the dashed line is for a compact star mass $1.4M_{\odot}$ and the dotted line is for the compact star mass $2.0M_{\odot}$. For the purpose of comparison, we plot the mass-radius curves for hydrogen main sequence star (solid line), helium main sequence star (dash-dot line; Verbunt 1990), brown dwarfs (dashed lines), and cold helium dwarf (dotted line). Similar to Markwardt et al. (2002), shaded contours represent lines of constant $\dot{M}_{\rm GR}$ (mass accretion rate, if the mass transfer is driven by gravitational radiation) for a $1.4M_{\odot}$ neutron star (Rappaport & Joss 1984). Brown dwarf models are for ages of 0.1, 0.5, 1, 5, and 10 billion years (from top to bottom). This figure demonstrates that the companion star in the source XTE J1814-338 is likely to be a bloated hydrogen main sequence star.

Table 1. Grid values considered for the parameters.

| Parameter | Grid values |
|--|---|
| R/M | 3.6, 3.8, 4.0, 4.2, 4.5, 4.8, 5.0, 5.2, 5.3, 5.5, 5.9 |
| $\phantom{aaaaaaaaaaaaaaaaaaaaaaaaaaaaaaaaaaa$ | 5°, 20°, 30°, 40°, 45°, 50°, 55°, 60°, 65°, 70°, 75°, 80°, 85°, 90° |
| $	heta_{ m c}$ | 10°, 20°, 30°, 50°, 70°, 90°, 110°, 130°, 150°, 170° |
| $\Delta \theta$ | 5°, 25°, 45°, 60° 0.0, 0.4, 0.42, 0.45, 0.48, 0.5, 0.52, 0.55, |
| n | 0.58, 0.6, 0.62, 0.65, 0.68, 0.7, 0.72, 0.76, 0.8, 0.85, 0.9, 0.95, 1.0, 1.5 |

Table 2. 90% confidence intervals for R/M and i.

| Parameter | EOS | Lower limit | Upper limit |
|-----------|--------------------|-------------|-------------|
| | $A18+\delta v+UIX$ | 4.0 | 4.7 |
| R/M | A18 | 3.9 | 4.7 |
| | B90 | 3.9 | 4.9 |
| | $A18+\delta v+UIX$ | 69° | 90° |
| i | A18 | 73° | 90° |
| | B90 | 73° | 90° |

Table 3. 90% confidence intervals for θ_c and $\Delta\theta$.

| Parameter | EOS | Burst group | Lower limit ^a | Upper limit ^a |
|----------------|--------------------|-------------------|--------------------------|--------------------------|
| $	heta_{ m c}$ | $A18+\delta v+UIX$ | Bursts: $1 - 8$ | 50° | 116° |
| | | Bursts: $9 - 16$ | 28° | 108° |
| | | Bursts: $17 - 22$ | $32^{\rm o}$ | 99° |
| | A18 | Bursts: $1-8$ | 61° | 120° |
| | | Bursts: $9 - 16$ | 40° | 110° |
| | | Bursts: $17 - 22$ | 50° | 149° |
| | B90 | Bursts: $1-8$ | 62° | 119° |
| | | Bursts: $9 - 16$ | 44° | 110° |
| | | Bursts: $17 - 22$ | 52° | 147° |
| $\Delta 	heta$ | $A18+\delta v+UIX$ | Bursts: $1-8$ | 35° | $\gtrsim 60^{\rm o}$ |
| | | Bursts: $9 - 16$ | 39° | $\gtrsim 60^{\rm o}$ |
| | | Bursts: $17 - 22$ | 39° | $\gtrsim 60^{\rm o}$ |
| | A18 | Bursts: $1-8$ | 25° | $\gtrsim 60^{\rm o}$ |
| | | Bursts: $9 - 16$ | $34^{\rm o}$ | 59° |
| | | Bursts: $17 - 22$ | 37° | $\gtrsim 60^{\rm o}$ |
| | B90 | Bursts: $1-8$ | 22° | 59° |
| | | Bursts: $9 - 16$ | $36^{\rm o}$ | $\gtrsim 60^{\rm o}$ |
| | | Bursts: $17 - 22$ | $38^{\rm o}$ | $\gtrsim 60^{\rm o}$ |

 $^{^{\}rm a}{\rm We}$ calculate the 90% confidence intervals for each burst group separately, because these parameters could in principle vary between bursts.

Table 4. Likelihood distribution of the beaming parameter n, combining data from all 22 bursts.

| Parameter | EOS: A18+ δv +UIX | EOS: A18 | EOS: B90 |
|-----------|---------------------------|-----------------------|-----------------------|
| n | Likelihood | Likelihood | Likelihood |
| 0.0 | 3.5×10^{-14} | 1.6×10^{-16} | 2.2×10^{-17} |
| 0.6 | 1.0 | 1.0 | 1.0 |
| 1.0 | 1.1×10^{-2} | 3.5×10^{-3} | 2.1×10^{-3} |
| 1.5 | 9.6×10^{-8} | 4.2×10^{-9} | 3.5×10^{-9} |

Table 5. Normalized likelihoods: comparison between two neutron star EOS models using the data from all 22 bursts of XTE J1814-338.

| EOS | Likelihood |
|---|--------------|
| $\begin{array}{c} A18 + \delta v + \text{UIX} \\ A18 \end{array}$ | 0.90 1.00 |